SCIENTIFIC REPORTS

OPEN

SUBJECT AREAS:
FLUID DYNAMICS
BIOPHYSICS
MOTOR NEURON
EVOLUTION

Received
4 August 2014

Accepted
1 September 2014

Published
23 October 2014

Correspondence and requests for materials should be addressed to P.R.B. (promode.bandyopadhya@navy.mil)

Modeling how shark and dolphin skin patterns control transitional wall-turbulence vorticity patterns using spatiotemporal phase reset mechanisms

Promode R. Bandyopadhyay & Aren M. Hellum

Naval Undersea Warfare Center, Newport, RI 02841, USA.

Many slow-moving biological systems like seashells and zebrafish that do not contend with wall turbulence have somewhat organized pigmentation patterns flush with their outer surfaces that are formed by underlying autonomous reaction-diffusion (RD) mechanisms. In contrast, sharks and dolphins contend with wall turbulence, are fast swimmers, and have more organized skin patterns that are proud and sometimes vibrate. A nonlinear spatiotemporal analytical model is not available that explains the mechanism underlying control of flow with such proud patterns, despite the fact that shark and dolphin skins are major targets of reverse engineering mechanisms of drag and noise reduction. Comparable to RD, a minimal self-regulation model is given for wall turbulence regeneration in the transitional regime—laterally coupled, diffusively—which, although restricted to pre-breakdown durations and to a plane close and parallel to the wall, correctly reproduces many experimentally observed spatiotemporal organizations of vorticity in both laminar-to-turbulence transitioning and very low Reynolds number but turbulent regions. We further show that the onset of vorticity disorganization is delayed if the skin organization is treated as a spatiotemporal template of olivo-cerebellar phase reset mechanism. The model shows that the adaptation mechanisms of sharks and dolphins to their fluid environment have much in common.

Sharks and dolphins are fast swimmers[1]. They have organized patterns of skin that stand proud[2–4]. Here, we carry out a spatiotemporal analytical modeling of the hydrodynamic interaction of these proud static and dynamic patterns with the surrounding water flow at low Reynolds numbers to understand the mechanisms causing the delays in onset of disorganization in the near-wall organization of fluid vorticity that allow sharks and dolphins to swim faster than would be possible otherwise.

The armor-like skin of sharks has two types of organization—a larger-scale nesting of tessellated dermal denticles (dd) on which three to six parallel riblets reside[2]. In the baseline turbulent boundary layers (TBL) over smooth surfaces, instabilities yield oscillations of two lateral wavelengths: one is manifested in streamwise streaks, and the other, which is a product of the interaction between the streaks and the mean flow, has a sub-streak wavelength[5]. These two wavelengths resemble those of the dd and riblets. The soft skin of dolphins, on the other hand, has arrays of lateral grooves and has been shown to vibrate via the underlying musculature[3,4,6–8]. Experiments show that a transfer of energy of flow instabilities to the damping surface stabilizes the flow[9,10]. Measurements on simulated riblets (sans dd)[11–13] and engineered compliant coatings[6,8,9,14] have been reported.

It is not known whether the seemingly disparate skin patterns of sharks and dolphins, and even their passive and active approaches, are in fact related to any universal mechanism of organizing the near-wall vorticity patterns or whether this mechanism is more extensively applicable to biological systems (Fig. 1). Here, we explore whether synchronization of oscillations in the lateral diffusion of vorticity is such a mechanism and whether there is a minimalist (systemic) mechanism of wall-turbulence regeneration that is amenable to analytical investigations of control. We discuss their relevance to very low Reynolds number wall turbulence.

Results

Hypothesis of organized skin patterning in sharks and dolphins. Many slow-swimming animals, such as seashells and zebrafish, have organized patterns of surface pigmentation, which, although flush with the surface, can be modeled as reaction-diffusion (RD) systems[15–19]. In these biochemical RD systems, two

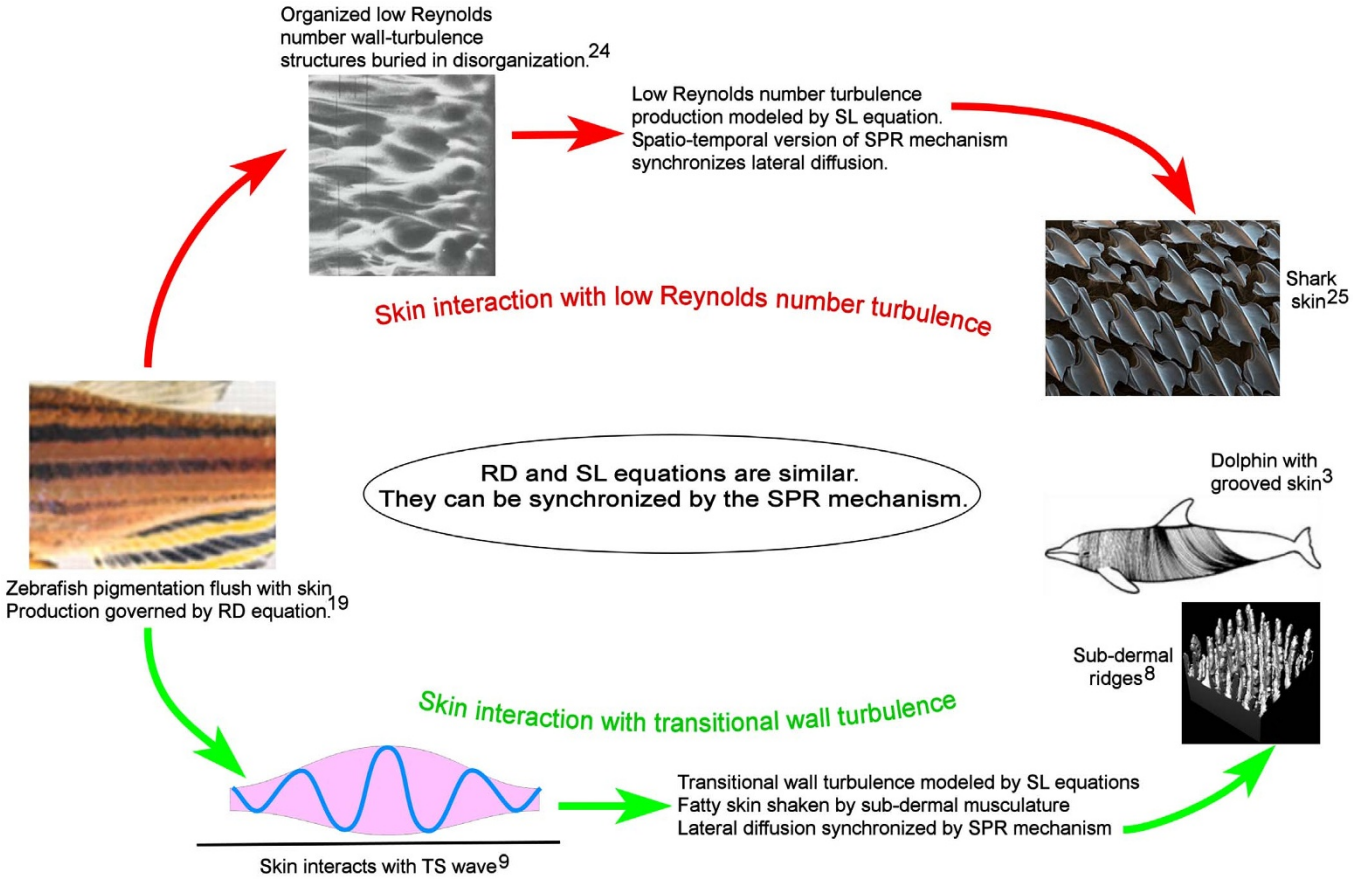

Figure 1 | Schematic of hypothesis of two different paths of evolution of shark and dolphin skins that are based on similar set of initial-condition dependent mechanisms. Abbreviations: RD (Reaction-Diffusion[15]), SL (Stuart-Landau[20]), SPR (Self-Referential Phase Reset[21,22]), and TS (Tollmien-Schlichting[6,9]). Fig. 1 left reprinted from Proceedings of the National Academy of Sciences with permission; Fig. 1 top left reprinted by permission of the American Institute of Aeronautics and Astronautics, Inc.; Fig. 1 top right reprinted with permission from NOAA Teacher at Sea; Fig. 1 right middle reprinted with permission from Institute of Electrical and Electronics Engineers; Fig. 1 right bottom © IOP Publishing. Reproduced by permission of IOP Publishing. All rights reserved.

substances diffuse at different rates to generate the stationary surface patterns. Experiments coupled to self-regulation modeling show[17,19] that, if the pigmentation is selectively ablated, the altered pattern forms the initial condition for a new pattern that is predictably generated, validating the underlying dynamic self-regulating nature. The broad success of describing the flush-skin pigmentation patterns of animals using the RD framework gives confidence that the raised skin patterns on sharks and dolphins may have evolved by simultaneous diffusion in the surface-normal and lateral directions to interact with the flow in a similar fashion. This is shown schematically in Fig. 1. Since RD systems are self-regulating, for control investigation, we take a universal approach by showing that the wall turbulence at transitional Reynolds numbers is also self-regulating in the spatiotemporal sense and can be described by SL equations coupled diffusively in the lateral direction to allow for growth in nonuniformities[20]. To control the onset of lateral and longitudinal disorganization in wall vorticity, we then make use of the self-referential phase reset (SPR) mechanism of synchronization found to be effective in olivo-cerebellar dynamics (modeled by FitzHugh-Nagumo (FN) equations, which are similar to SL equations) and which controls muscle coordination to generate the motion of animals[21–23].

A restricted model of wall-turbulence regeneration cycle at transitional Reynolds numbers. Since experiments[24,26–32] on flat-plate TBL have demonstrated that, submerged in the seeming randomness, a spatiotemporal organization of near-wall vorticity patterns exists, the instability process of turbulence regeneration must be laterally coupled. Here, a systemic model of near-wall turbulent flow is first developed that reproduces many of these observations of organized vorticity patterns at transitional and low Reynolds numbers. This model is confined to a single near-wall plane where turbulence production is known to reach a maximum, and it is concerned only with the pre-breakdown durations of production cycles, when the fluid is dominated exclusively by molecular, rather than so-called "eddy," viscosity. Francis Hama[26], who discovered the ubiquitous wall streaks in near-wall turbulence, did attempt to model their formation as distortions in lateral vortex lines, which are similar to the pigmentations on seashells. The approach was not pursued, we believe, because it was not analytically related to the earlier observations of quasi-cyclicality by Einstein and Li[33], and a formal self-regulation model of regeneration was not developed. Dynamical systems theories were developed later.

The idea of separating pre- and post-breakdown regimes (Fig. 2) originates in the observation[33] of a near-wall, quasi-cyclic process wherein a viscous-dominated sublayer thickens at declining rates and then abruptly undergoes breakdown into turbulence and collapses. We interpreted this process as the sublayer undergoing a self-regulating growth-decay cycle wherein the vorticity accumulated during growth is abruptly liquidated into Strouhal arrays of hairpin vortices lifting off from the wall due to induction of the image vortex[29,31,32]. The thickness at which the breakdown occurs marks a point of bifurcation, such that the dominant forces acting on the fluid change from being primarily due to molecular viscosity to

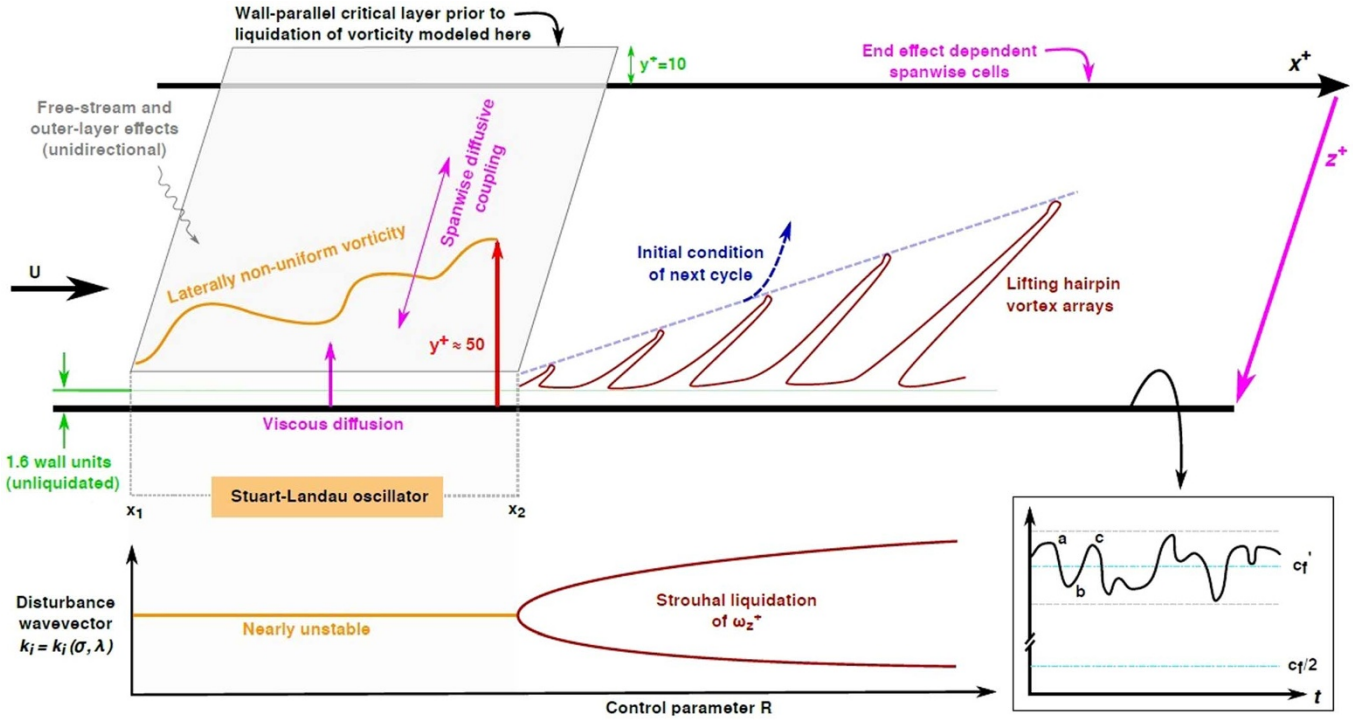

Figure 2 | Separation of near-wall TBL into pre-breakdown (no hairpins) and post-breakdown (with hairpins) regimes, dominated by molecular and eddy viscosity, respectively. Inset: Turbulent skin friction (c_f') is self-regulated between limits; the lower limit may drop to a minimum of $c_f/2$.

predominantly due to turbulent mixing. This distinctly two-phase alternating behavior in the same spatial region suggests that a well-known phenomenological model such as the Ginzburg-Landau (GL) theory[34] could reproduce many of the relevant flow features. In the present work, we use SL equations instead because they have been found to be useful in fluid dynamics[20,35].

To understand the mechanism by which sharks and dolphins might possibly be controlling the vorticity patterns, we note that a spatially uncoupled assembly of FN neurons that individually appear weak and noisy can be made to temporally phase-synchronize[21,22] in response to an external temporal impulse (I_{ext}) of the correct amplitude and duration, a process known as SPR. The SL equations employed are amenable to SPR-like control whereby the animals' patterned skins are altering the characteristics of the viscous-dominated pre-breakdown fluid very near the skin surface by (1) imposing weak spatial perturbations to the diffusive characteristics and (2) applying time-periodic inputs to the system. The latter mechanism is essentially Llinás's neuron synchronization[21] generalized to a spatially coupled system and has been established in other systems[36]. Spatiotemporal pattern control using spatial inhomogeneity has been proposed in the context of morphogenesis[18]; the present work explores whether these strategies enable an effective means of control by sharks and dolphins over the chaotic behavior of the turbulence near their skins. Our model may be useful in the analytical exploration of new strategies of artificial skin design since no such tools exist today.

Fig. 2 shows the pre- and post-breakdown regimes of the three-dimensional boundary layer growth and breakdown cycles and shows the near-wall parallel layer to which the model is restricted. The pre-breakdown regime is characterized by vorticity that is diffused but three-dimensional. The breakdown is an abrupt liquidation via Strouhal shedding of hairpin vortices[29,31,32]. This liquidation reduces the thickness of this layer to about 1.6 wall units[37]. The post-bifurcation regime is responsible for turbulent mixing characterized by eddy viscosity; the present work does not attempt to model this regime but focuses instead on the spatiotemporal instabilities of the pre-bifurcation regime, where the matters most important to disorganization control occur.

It can be argued that the turbulent part of the skin friction c_f' in the Fig. 2 boxed inset where a-b-c… represents decay and growth cycles, systemically undergoes self-regulation and oscillates between the dashed lines. Compare the systemic linear and nonlinear processes as follows. A linear process with frequency ω and damping ζ, such as $\ddot{c}_f' + 2\zeta\omega\dot{c}_f' + \omega^2 c_f' = 0$, converges for $\zeta > 0$, diverges for $\zeta < 0$, and oscillates for $\zeta = 0$. Since the effect of the initial condition (IC) on the system c_f' is proportionate, the oscillations are large or small depending on the IC. In contrast, the process $\ddot{c}_f' + 2f(c_f')\dot{c}_f' + \omega^2 c_f' = 0$ with nonlinear damping $f(c_f') = a_0 c_f'^2 - 2\zeta_0\omega$ will oscillate continuously as in the inset. In this latter expression, the effect of the damping is negative when c_f' is small for $(a_0, \zeta_0) > 0$ and positive when it is large. The constants a_0, ζ_0, and ω determine the size and shape of the limit cycle. The SL equations employed in the present work are one example of a nonlinear process. Due to lateral diffusive coupling, the oscillations in the inset look random, and we explore whether such randomness can be removed by synchronization.

Restricted SL equation modeling of how wall vorticity becomes disorganized at low Reynolds numbers. From the Navier-Stokes equations, Stuart[38] and Watson[39] showed that small disturbances $A(t)$ in parallel (e.g., Couette, Poiseuille) flows near the critical Reynolds number Re_{crit} evolve via the Stuart-Landau (SL) oscillator equation, Eq. (1):

$$\dot{A} = \sigma A - \lambda A^2 A^*, \tag{1}$$

where A is any physical quantity indicated by the Navier-Stokes equations[35], and $\dot{(\cdot)}, (\cdot)^*$ indicate time derivative and complex conjugate operations, respectively. The complex coefficients σ, λ are determined by the flow and modeled quantity. The model is applicable to nonparallel flows if the flow development time scale is slow compared with that of perturbation growth. The requirement that $Re \approx Re_{crit}$ is satisfied within the pre-breakdown fluid because liquidation occurs when a layer of that fluid is sufficiently thick (about 50 wall units).

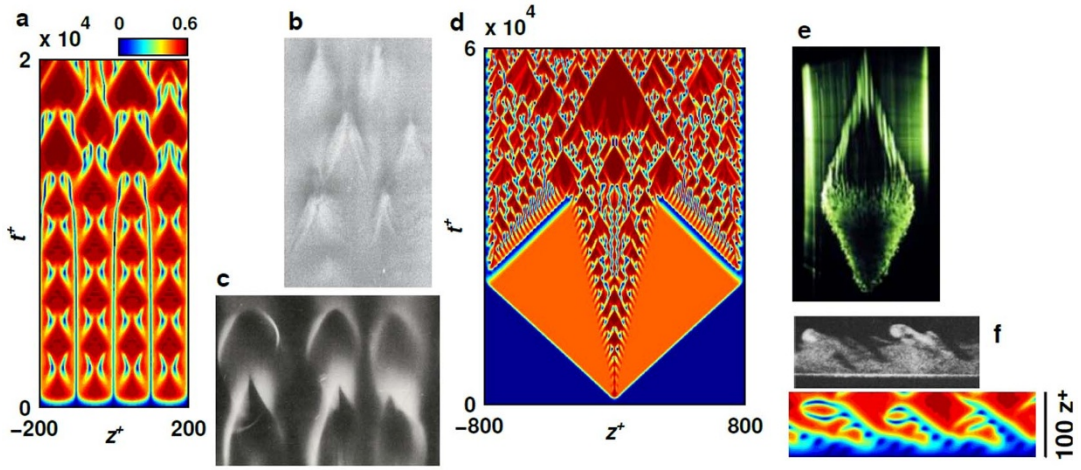

Figure 3 | Transitional flow comparison between model and experiments. (a), (d), (f lower) Modeled transitional flow. (b[44]), (c[45]), (e), (f upper[29]) Transitional flow observed in experiments. Emmons' turbulence spot dye-visualization (e) due to M. Gad-el-Hak, *Pvt. Comm.* d: $k_x = 0$, $\mu = 16(1 + 0.1i)$, $\lambda = (1 - 2i)/A_0$. Fig. 3b reprinted by permission of the American Institute of Aeronautics and Astronautics, Inc.; Fig. 3c reprinted by permission of the Cambridge University Press; Fig. 3e reprinted by permission of M. Gad-el-Hak; Fig. 3f reprinted with permission of the Cambridge University Press.

Spanwise diffusive coupling can be introduced into Eq. (1), such that

$$\dot{A}(z,t) = \sigma A + \mu \frac{\partial^2 A}{\partial z^2} - \lambda A^2 A^*. \qquad (2)$$

Coupling in this form was used to model bluff body vortex shedding and the growth of chevron patterns in the cylinder wake[35,40].

SL oscillators can be used to model different states, structures, and their coupling. For example, relating to familiar properties, the modified SL expression $\dot{\delta}_s^+ = \left(\frac{\beta}{\Re(\delta_s^+)} + \sigma\delta_s^+ - \frac{\lambda}{d_\delta} \left|\delta_s^+ - \kappa\right|^2 (\delta_s^+ - \kappa) \right)$ can be used to model the thickness of the unsteady viscous layer (which extends up to where the mean buffer layer merges with the log layer), where[41] $\beta \approx 6.64$ and the SL constants σ and λ are as described in Methods. The coefficients $d_\delta = 2400$ and $\kappa = 53 + 20i$ determine the shape of the limit cycle. Here, i and $\Re$ are imaginary and real, respectively. In the equation above, the sublayer thickness δ_s^+ oscillates between 2 and 57, as known[37,41]. The finite lower limit satisfies the observations and the theory of separation[42,43]. The upper limit denotes the onset Reynolds number (Re_{crit}) of vorticity liquidation into hairpin vortices. Uncontrolled lateral diffusion would blur the limit cycle. The vorticity models, their description, the calibration of the constants employed, the simulation parameters, and the control equations are provided in Methods.

Comparison between model and experiments in laminar-to-turbulent transitional regimes. Fig. 3 shows that the model reproduces approximate vorticity distributions obtained using different means of visualization. Figs. 3a–3c show the arrayed and staggered patterns known as K- and H-types, respectively[44]. The Emmons turbulence spot is compared in Figs. 3d–3e, where Fig. 3d is produced by an initial condition of a spike in the input vorticity distribution at $(z^+, t^+) = 0$. In the Fig. 3f lower plot, the vortex shedding in the smoke-flow visualization figure (upper plot) was modeled by applying a corner boundary condition. Time t^+ in theory and distance x^+ in smoke or dye flow visualization (which is a time history and is like a strip-chart record) are positive in opposite directions[35]. There is remarkable agreement in all cases. In Fig. 3f, the curling and inclinations of the hairpins are identical (a transformation between t^+ and x^+ is made). While the momentum thickness Reynolds number of the TBL in the Fig. 3f upper plot is low (500), the curls appear throughout higher-Reynolds-number TBLs and are regions of high Reynolds stresses[24,29]. This suggests that extension of the model to the post-breakdown mixing region in the future may be feasible.

Figs. 3 and 4 show baseline validations of the minimal model—without control. The disorganization in Figs. 3d and 4a looks daunting from a control point of view. To clarify, modeling of the baseline organization is not the goal. The goal is to show (see Figs. 5 and 6) how sharks and dolphins, in spite of their seemingly disparate appearance, use essentially the same mechanism to delay the onset of such disorganization.

Comparison between model and experiments in the very low Reynolds number but fully turbulent regime. In Figs. 4a–4c, it is shown that the laterally coupled SL model yields chaotically-masked organized patterns of $\left|\omega_z^+\right|$ that are strikingly similar to those observed via near-wall smoke visualization[24] and in the pattern of shark dermal denticles[46]. Fig. 4d shows two types of $\left|\omega_z^+\right|$ patterns: as shorthand, we have designated the quasi-aligned patterns of smaller-delta structures as "A-patterns" and the generally staggered patterns of larger triangular structures (called subharmonics in transition[44]) as "S-patterns". In Fig. 4d, the accumulation of small S- and A-patterns eventually yields a large S-pattern, which then collapses; this is depicted as a competition between positive and negative feedback processes in the schematic in Fig. 4e[17,19,47]. The widely prevalent wall-parallel inclined waves in each subharmonic (red triangles in Fig. 4d) are produced when localized disturbances of different wave velocities are created (at the tips of the triangles). For comparison, note that control of inclined waves[48] has been shown numerically to reduce drag.

In biological systems, groups of patterns similar to the one in Fig. 4d become unstable because the diffusion of the antagonist (negative feedback) is slow[16]. The interactions of the S-and A-patterns are similar to two chemicals interacting in a self-regulating manner as given, essentially, by Turing's[15,19] RD equations. As Figs. 5 and 6 will show later, the onset of chaos can be controlled in the present system by spatiotemporal management of the diffusion in a manner consistent with the skin patterns found on sharks and dolphins.

The pre-breakdown nucleation sites of hairpins are shown using smoke visualization[24] in Fig. 4f, along with a sample (subharmonic) S-pattern (frame C in f) from the present model. The similarity between section A-A in Fig. 4f and frame C indicates that the "base" of the S-pattern likely forms the near-wall end of an incipient hairpin vortex.

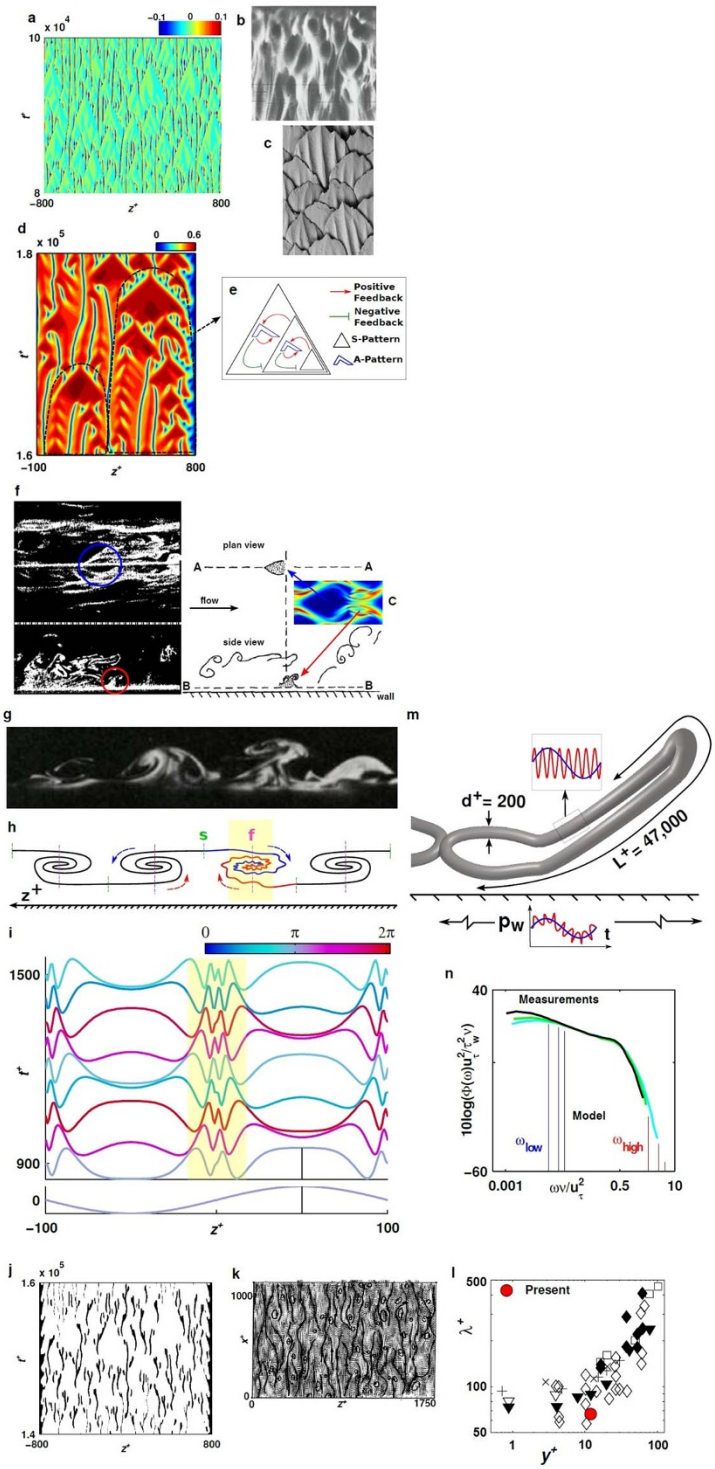

Figure 4 | Comparison to visualization and skin topology. (a) $\partial\phi(\omega_z^+)/\partial z^+$ obtained via present model. (b) Smoke trace visualization[24]. (c) Great white shark dermal denticles[46]. (d) $|\omega_z^+|$ pattern ($\mu_r = \mathbf{64}$) interaction is a series of interacting feedback mechanisms (e). (f) Pre-breakdown hairpin nucleation sites observed[24] at base of S-patterns ($y^+ = 9$–14) via simultaneous parallel (top) and longitudinal (bottom) smoke visualization. Inset (C) S-pattern from present model. (g) Cross-stream smoke visualization[45] in transitional boundary layers. (h) Schematic explaining (g) and (i), where s (green) is a saddle and f (red) is a focus. (i) Crashing diffusion waves collecting at a focus form carrier waves; scale bar $= \mathbf{2}(\sigma_r/\lambda_r)^{1/2} = 1.2$. (i lower graph) Initial Condition; scale bar $= 0.2$; variable: $\boldsymbol{Re}(\omega_z^+)$, $\mu_r = 0.5$. Color: $\phi(\omega_z^+)$ at $z^+ = 50$. (j) Streaks $(|\omega_z^+| < 0.3)$ from model, $k_x = \mathbf{0}$, $\mu = \mathbf{16}(\mathbf{1} + \mathbf{0.1}i)$, $\lambda = (\mathbf{1} - \mathbf{2}i)/A_0$. (k) Streaks observed by PIV[49]. (l) Streak spacing via present model (red-filled circle) and via literature[49] (other symbols). (m) Schematic of origin of wall-pressure fluctuations (p_w) showing vortex-tube waveguide model of resonance. (n) Modeled resonance frequencies (ω_{high}, ω_{low}) compared with measurements[50] of spectra ($\phi(\omega)$) in TBL of high momentum thickness Reynolds number (Re_θ); three vertical lines in each of the ω_{high} and ω_{low} ranges, respectively, represent (from left to right) oscillation modes 1, 2, and 3, respectively. Fig. 4b & 4f (except inset C) reprinted by permission of the American Institute of Aeronautics and Astronautics, Inc.; Fig. 4c reprinted with permission from T. Sewell and M. Waldron; Fig. 4g reprinted by permission of the Cambridge University Press; Fig. 4k & 4l reprinted with permission from R. J. Adrian; Fig. 4n reprinted with permission from J. B. Forest.

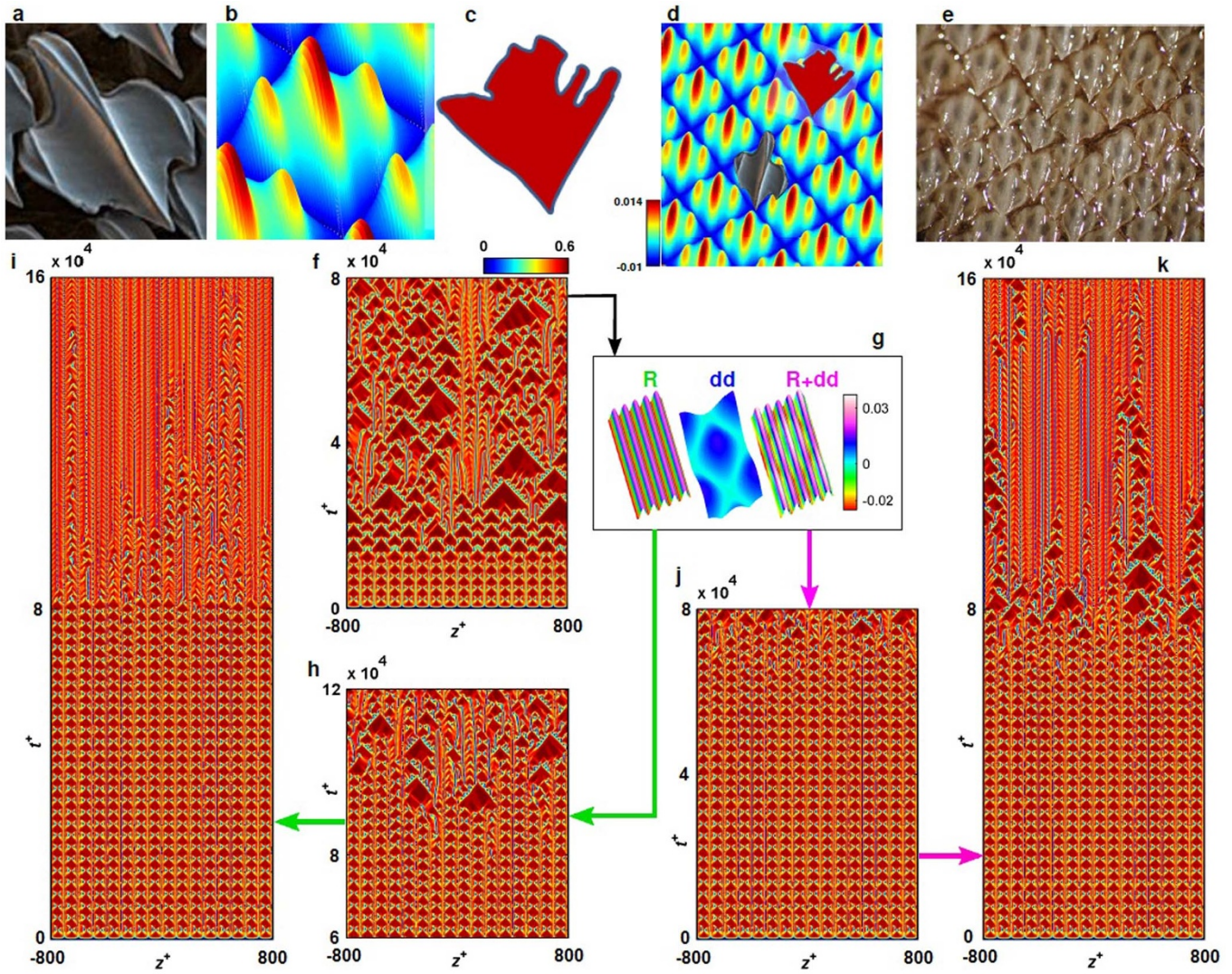

Figure 5 | Shark skin is a template of organized diffusion for control of disorganization. (a) Atlantic sharpnose dd[25]. (b) Diffusion template. (c) Single element of S-pattern. (d) Modules a and c on arrayed diffusion template. (e) Staggered tiger shark dd[2]. (f) and (h)–(k) are $|\boldsymbol{\omega}_z^+|$ maps. (f) Baseline (no surface variation). (g) $\boldsymbol{\mu}_r$ analog of surface; R, dd, and R + dd refer to riblets, dermal denticles, and their combinations, respectively. (h) Uninterrupted weak riblets. (i) Combination of uninterrupted weak ($t^+ < 80{,}000$) and strong ($t^+ \geq 80{,}000$) riblets. (j) Weak riblets combined with dd. (k) Weak, then strong, riblets as in (i), combined with dd. Fig. 5a & 5d lower inset reprinted with permission from NOAA Teacher at Sea; Fig 5e reprinted with permission from M. S. Adams.

A cross-stream smoke visualization[45] of tilted, near-surface "mushrooms" is shown in Fig. 4g, with arrows indicating the direction of secondary flow in this plane. The head of the mushroom consists of a single saddle (**s**) from which smoke diverges and two foci (**f**) where it is collected. The lower saddle, shown schematically in Fig. 4h, is not visible in the experiment; it is likely to be more diffused, owing to its wall proximity. The time development of a pair of transverse diffusion waves that matches the mushroom development is shown in Fig. 4i: the diffusion waves approach each other laterally, slow down, and break up into small wavelength oscillations (see the video in Supplementary Information (Movie 1)). These short-wavelength waves are co-located with the long streaks observed in Figs. 4i, 4j, indicating that the low-frequency streaks are behaving as long solitary waves upon which the high-frequency carrier waves ride. The short wavelengths form better after antagonistic waves have crashed into each other, when the wavelength of the initial $\omega_z{}^+$ vorticity is 200 z^+. The model shows that streak formation and coupling[51–53] of large and small wavelengths (or frequencies) are related processes.

The small wavelengths in Fig. 4i have the approximate amplitude (and meandering) of $10z^+$, which is the optimal riblet wavelength. Both the streak and the sub-streak wavelength are present in this figure.

The basic frequency of the oscillations in Fig. 4i is 100 π. This basic frequency is akin to the TS frequency, in that it is the frequency of the most unstable wavelength in the sublayer. It has been shown[41] that the unsteady sublayer velocity profile approaches the Blasius[54] form just before breakdown and can be expected to be amenable to the brief production of nearly two-dimensional oscillations. Since the TS frequency is the natural frequency of the most unstable wavelength in the pre-breakdown fluid, the carrier wave can be thought of as an orthogonal TS wave—an unstable perturbation in the transverse diffusive waves. The viscous cores of the streaks indicated by **f** in Fig. 4h, and shown in Figs. 4d and 4j, locally produce a low pressure. Co-location of these cores with the carrier waves would indicate that this low pressure will be modulated at high frequency. This high frequency could be localized by an animal using highly tuned tactile pressure sensors; the compactness of the carrier wave in frequency space means that a large sensor gain could be achieved.

An experimental observation[49] of near-wall streaks using particle image velocimetry (PIV) is provided in Fig. 4k. The authors of that

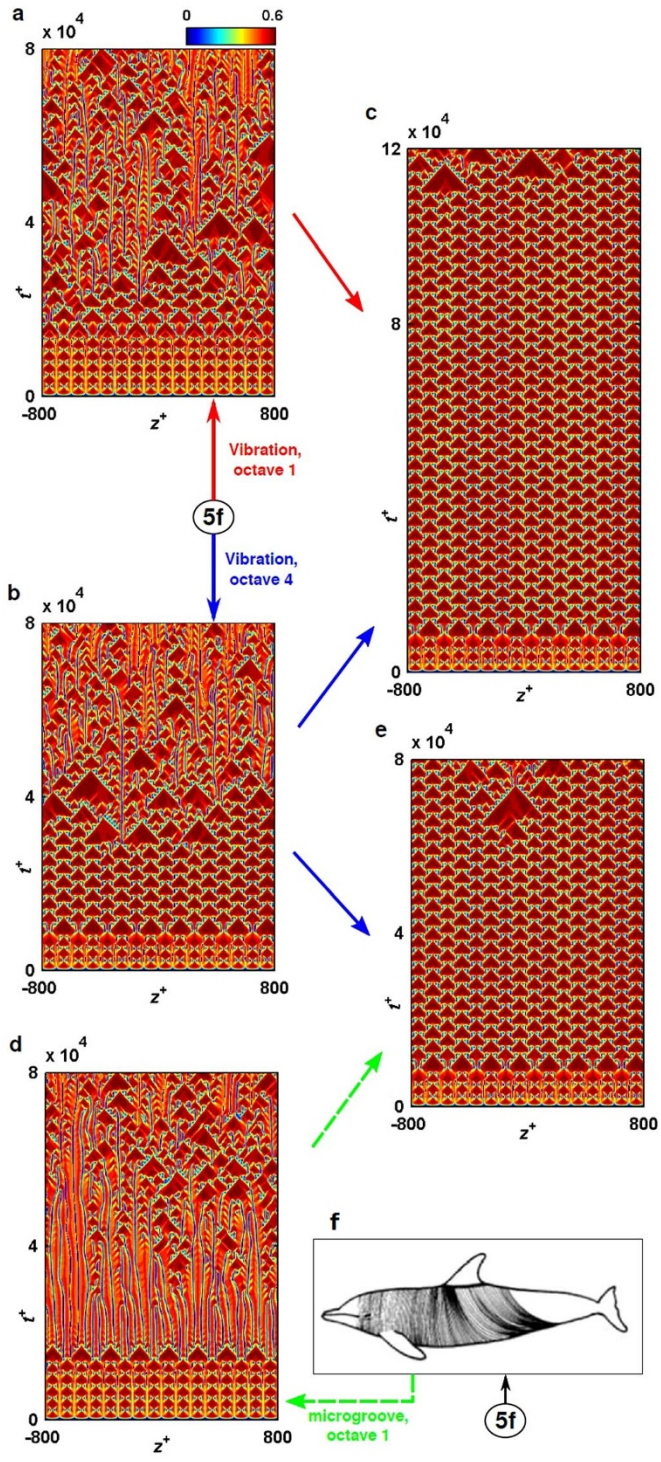

Figure 6 | Dolphin control of disorganization using microgrooves and vibrations. (a)–(e) are $|\omega_z^+|$ maps; Fig. 5f is the baseline. (a) Fast vibration, frequency is groove wavelength, which is also the primary SL wavelength. (b) Slow vibration, frequency is groove wavelength/16. (c) Combines (a) and (b). (d) Microgrooves at basic oscillator wavelength. (e) Combines (b) and (d). (f) Sketch of dolphin microgrooves[3]. Fig. 6f reprinted with permission from IEEE.

work provided streak spacing data from a variety of published sources, which are reproduced and compared with our findings in Fig. 4l. These data are used to determine the approximate aspect ratio of the modeled fluid and, thereby, the baseline value for the diffusion coefficient μ (see Methods).

In the unstable wall-parallel layer at $y^+ \approx 11$, the unsteadiness of the pre-breakdown viscous flow is modeled by a parabolic equation[54] (Eq. (2)). The reversal of the lateral direction of vorticity diffusion (Fig. 4i) gives rise to rows of stagnation points appearing as streaks and to dislocation sites where streaks merge or diverge. (The reversal of vorticity diffusion is modeled by singular parabolic equations.) The boundaries where the diffusion changes sign are regions of large variation in tracer concentration and density and where disorganization likely ensues. The surface templates in the shark/dolphin model control the motion of the stagnation points, thus restricting the diversification of scales, and this is more feasible at low Reynolds numbers.

The effects of side walls and variations in initial conditions (indicative of three-dimensional effects or incoming turbulence) yield changes in the precise route to disorganization in the $(\omega_z^+ - t^+)$ maps but no qualitative change in the basic spatial organization of ω_z^+ patterns. In addition to the corner boundary conditions (see Methods), these effects were modeled as variations in initial wavelength from $z^+ = 50$–800 and higher, to 0.01% random variation in the amplitude of $\omega_z^+(0,z^+)$, respectively. The results presented here are indicative of a low Reynolds number, since perturbations from beyond the modeled region have been neglected. The basic regeneration phenomenon underpinning the model is likely to be robust at higher Reynolds numbers as well; the periodic liquidation of a near-wall sublayer into hairpins has been observed at Reynolds numbers much higher than transition[29,31,32,55]. The delay of chaos onset shown by our modeling of synchronization likely became possible because the bandwidth of the spatiotemporal variation is restricted at low Reynolds numbers.

An alternative phenomenological model of the results in Fig. 4i (presence of high-low frequencies). The intriguing simultaneous observations of high and low frequencies throughout a TBL[51–53], and the modeled formation of large-wavelength streaks and small-wavelength, seemingly resonant waves due to crashing lateral diffusion (Fig. 4i, Movie 1 in Supplementary Information), can be reproduced using a different phenomenological approach, namely a waveguide model of wall-pressure fluctuations (Fig. 4m,n). This is an indirect but independent corroboration of this result of the model and is given below.

From the converging/diverging dislocation singularities, a pair of streaks and hairpins (they have viscous cores) forms a closed, laminar, viscous, resonant "cavity" (strictly speaking, the cavities are partially connected) (Fig. 4m). We draw an analogy to Schumann resonance in the ionosphere cavity and replace the speed of light with that of sound, the earth's circumference with the hairpin vortex tube length, and the ionosphere's height with the vortex tube diameter. Two disparate groups of resonant pressure waves—one large and one small—are produced by the cavity length and diameter as $\omega_n \upsilon / U_\tau^2 = \left[c^+ / (\Lambda^+)\right] \sqrt{n(n+1)}$, where ω_n is angular frequency, c^+ is the ratio of the speed of sound in the medium c to the friction velocity U_τ, $\Lambda^+ = \Lambda U_\tau / \upsilon$ is the length L^+ or the diameter (d^+) of the cavity, n is the mode, υ is viscosity, and U is velocity scale. Losses and leaks to other cavities would reduce the measured frequencies and widen the spectral peaks, but the resonance would be long-lasting, yielding a spatiotemporal/TBL pressure fluctuation with two regimes of wall pressure spectral density (PSD) $\Phi \propto \omega_n^{-N}$, where N is a different constant in the high- and low-frequency ranges of resonance. The waveguide model explains why there is a clear kink in the PSD and Reynolds number independence (Fig. 4n). Typically, for a streak length of 1000 wall units (Fig. 4m) and $\delta^+ = 15{,}800$ at a momentum thickness Reynolds number[50] of 36,000, $L^+ = \frac{LU_\tau}{\upsilon} = 47{,}000$ (considering hairpins inclined at 45° to the flow direction), and $d^+ = 200$ wall units. For $n = 1$ to 3, the model yields $\frac{\omega_{low} \nu}{u_\tau^2} = 0.0102$–$0.0250$

(<0.5), and $\frac{\omega_{high}\nu}{u_\tau^2} = 2.37–5.81$ (>0.5). Compared with the time-averaged wall-pressure measurements of PSD, these values correctly lie in two distinct Reynolds-number-independent PSD decay regions, with the slope changing abruptly near $\frac{\omega\nu}{u_\tau^2} = 0.5$. In contrast with prevailing notions, ω_{high} may be sourced from anywhere in the rotational TBL, and ω_{low} may be sourced solely from the society of interconnected wall streaks without the hairpins.

The present waveguide model implies that, for bifurcation control, the animal skins are prescribing the length, diameter, and modes of pressure oscillation in the streaks and hairpin vortices.

Modeling of delay in onset of disorganization in wall vorticity by shark skins. Fig. 5 shows the results of the modeling of chaos control by sharks. Skins of great white[46], Atlantic sharpnose[25], and tiger shark[2] dermal denticles (dd), with embedded riblets, are shown in Figs. 4c, 5a, and 5e, respectively. The model uses a periodic distribution in (z^+, t^+) or (z^+, x^+) of the coefficient of lateral diffusion, which we call "μ-control." Examples of these distributions are shown in Figs. 5b, 5d, and 5g. These diffusion templates were created to be similar to the topology of a shark's skin; the topology alters the local aspect ratio of the pre-breakdown layer, which is reflected in the diffusion coefficient (see Methods).

Fig. 5f shows the development of disorganization in a TBL, wherein an aligned pattern consisting of organized S- and A-patterns gives way to a staggered pattern at $t^+ \approx 10{,}000$, which shortly thereafter becomes chaotic. Fig. 5g is a contour map of the lateral diffusion used to model riblets (R), the dermal denticles (dd), and their combination (R + dd). The details used to describe the R, dd, and R + dd surfaces are provided in Methods. At the uninterrupted riblet spacing of 10 z^+, weak lateral diffusion perturbations of 2.5% ("weak riblets") delay the onset of chaos, and the aligned pattern is conserved for $t^+ \leq$ 80,000 (Fig. 5h). If a 20% perturbation ("strong riblets") is then applied at $t^+ \geq 80{,}000$, a different orderly pattern, consisting almost entirely of streaks, is produced (Fig. 5i). The initial delay of the onset of disorganization requires only weak perturbations, but it does not perfectly control all deviations from the aligned pattern.

As these small uncontrolled deviations grow, a Reynolds-number-like effect is produced (see also Fig. $7D_2$ in Kazantsev *et al.*[21]) that requires larger diffusion perturbations to control[41].

The need for the animal to flex requires that the riblets be interrupted along the dd outlines shown in Figs. 4c, 5d, 5e, and 5g. Figs. 5j and 5k show the combined effects of weak riblets that are interrupted by the dd without and with, respectively, inclusion of strong riblets for $t^+ \geq 80{,}000$. Using the present model, the dd are not found to delay the onset of disorganization, but their interruption of the riblets does not qualitatively change the riblets' ability to control the disorganization. The combined effect of the riblets and dd is the method of disorganization control that we predict is being employed by sharks.

Modeling of dolphins' control of the onset of disorganization in wall vorticity by using wall vibrations and microgrooves. Fig. 6 shows the results of the modeling of disorganization control by dolphins. The baseline surface shown in Fig. 5f is the pattern that is being controlled. Dolphins' lateral microgrooves[3] (Fig. 5f) employ μ-control with a wavelength equal to the groove wavelength; this control strategy is similar to the sharks' control strategy shown in Fig. 5. Applied in isolation, this strategy strongly enhances streak formation for $t^+ < 30{,}000$, with effects persisting locally out to $t^+ \approx 80{,}000$.

Active vibration of the surface is modeled as an external input to the oscillators, which we call "I_{ext}-control". These skin vibrations have been recorded *in vivo*[4]. This external input is added in two integer multiples of the primary SL wavelength, which is also the groove wavelength; Figs. 6a and 6b represent multiples of 1 and 16, respectively. Combined application of these vibrations yields a significantly improved result, shown in Fig. 6c. Unlike the aligned results found for the optimal shark skin surface, this "multiple octave" control strategy creates a staggered array of S-patterns, persisting until $t^+ \approx 110{,}000$. The diffusive and vibrational control strategies can also be combined, as in Fig. 6e, where the long-wavelength vibration is paired with the microgrooves. This also yields a staggered S-pattern array. Details of these control strategies are provided in Methods. Following Lighthill, the vibrating wall ($\dot{L}$) will cause acoustic radiation (p_w) (L is load and p_w is wall-pressure fluctuation), and an audible analogy, called E-5 by musicians and produced using a guitar, is given in the Supplementary Audio Recording 1 (SI).

Dolphins' soft, fatty skin is well-suited to the application of surface vibration from the underlying musculature[4,7,8], whereas sharks' denticles and riblets are made of a rigid, tooth-like material that is less suited to this type of subsurface input. Our search did not find that global external perturbation added to the riblet + denticle combination employed by sharks improved the surface's ability to control disorganization. However, streak spacing can be organized by localized I_{ext} if sensors are used to identify streaks[41]. It will be interesting to know whether shark skins, in spite of their armor-like appearance, are populated with wall-pressure sensors and have the ability to vibrate their skins.

Similar to the riblet diffusion template employed by sharks, the dolphins' lateral microgroove template and weak vibrations are comparable to the olivo-cerebellar temporal SPR mechanism[21,22]. However, in the turbulence control employed by these animals, the spatial locations and coupling of the vorticity oscillators is important, which was not the case for the temporal synchronization of inferior-olive neurons. The present work advances the SPR technique to spatial problems.

Discussion

The feasibility and cost of control are as follows. The Reynolds numbers of whales (up to blue whales: $0.4–3 \times 10^9$) and dolphins ($0.2–1.75 \times 10^8$) are similar to those of ships/submarines ($>2 \times 10^9$) and unmanned underwater vehicles ($>2 \times 10^7$), respectively. Consequently, the feasibility of cost-effectively delaying the onset of vorticity disorganization near the nose of practical flows should not be in doubt.

Although Newton's laws of motion apply at all instants of time, in wall-turbulence modeling, time averaging is widely used to reduce information overload, although there is no instant of time when any dynamical state adheres to the modeled distributions. On the other hand, the volume of information in spatiotemporal approaches can be large. For example, there are numerous oscillations in Fig. 5f, and the cost of controlling each of them would seem to be large. However, the present SPR-synchronization model shows that, for dolphins, external perturbations of only two specific wavelengths are adequate for delay of chaos onset. Hence, the cost will be lower than thought by past researchers. At least at low Reynolds numbers, the spatiotemporal analysis of control is found to be instructive.

Full-scale animal swimming[20] can be modeled as a resonant oscillatory structure where the quality factor of the tuning is high (low damping in the narrow frequency range of oscillation). Since the present modeling of the phenomenon of near-wall transitional turbulence is similar, the active vibration (I_{ext}) of a high-quality-factor dolphin skin in a narrow band would cost less than in a skin which is broadly vibrated.

Our minimal model shows that a part of the low Reynolds number wall-turbulence that is critical to reproduction can be treated as systemically deterministic for control purposes. This result has significance to many aspects of future research—in full modeling, diagnostics, and control.

Methods

The restricted near-wall TBL model. Spanwise and streamwise vorticity perturbations, ω_z^+ and ω_x^+, respectively, were modeled by the SL equations

$$\dot{\omega}_z^+ = \left(\sigma\omega_z^+ + \mu\frac{\partial^2\omega_z^+}{\partial z^{+^2}} - \lambda^z\omega_z^{+^2}\omega_z^{+^*} - k_x\left|\omega_x^+\right|\right)\tau, \qquad (3)$$

$$\dot{\omega}_x^+ = \left(\sigma\omega_x^+ + \mu\frac{\partial^2\omega_x^+}{\partial z^{+^2}} - \lambda^x\omega_x^{+^2}\omega_x^{+^*} + k_z\frac{\partial\omega_z^+}{\partial z^+}\right)\tau, \qquad (4)$$

where τ is a time scaling, and k_x, k_z are positive, real coupling constants. $(\cdot)^+$ indicates a quantity in wall units. The coupling mechanism indicates a sink in ω_z^+ scaling with ω_x^+, and a source in ω_x^+ consistent with continuity, assuming that $\omega_y^+ \ll \omega_x^+$ and $\partial/\partial x \approx \kappa\,\partial/\partial t$. We call this an "orthogonal" coupling due to this consistency with continuity. The simplest mechanism meeting these requirements was chosen, but others exist.

Parameter estimation. The SL oscillator in Eq. (3) has base amplitude $A_0 = (\sigma_r/\lambda_r^z)^{1/2}$ and spanwise scale proportional to $(\mu_r/\sigma_r)^{1/2}$. Near the wall, the wall-shear stress $\tau_{wall} \approx \omega_z$, since $dv/dx \approx 0$ (v is the surface-normal velocity). The quantity $\tilde{\tau}_{wall}/\overline{\tau}_{wall}$ is in the range[56] of 0.32–0.40, where $\widetilde{(\cdot)}$ and $\overline{(\cdot)}$ are the standard deviation and mean, respectively. In the present model, $A_0 = 0.63$ yields $\tilde{\omega}_z^+ = 0.364$; $\bar{\omega}_z^+ = 1$ by definition. For $\sigma = \sigma_r(1 + c_0 i)$, $\mu = \mu_r(1 + c_1 i)$, $\lambda^z = (1 + c_2 i)/A_0^2$, we employ[35] (unless noted) $c_1 = 0.3$, $c_2 = -3$. $c_0 = 1$ yields unit linear frequency.

Unless noted, the spanwise scaling factor $\mu_r = 16$. This is estimated from[35] $\sigma_r - \mu_r(\pi/L_c)^2 = s(Re - Re_{crit}) = 0$ for characteristic aspect ratio L_c. $Re = Re_{crit}$ is assumed, per the self-regulating nature of the sublayer. L_c is the ratio of near-wall streak spacing to measurement layer height (Fig. 4l and Ref. 49). The best fit for points in the range $0 \le y^+ \le 50$ is $\mu_r = 467.7(y^+)^{-1.62}$. Using this fit, $\mu_r = 16$ corresponds to $y^+ = 8.10$, near the range $9 \le y^+ \le 14$, indicated by comparison of our results with spatio-temporal observations[24].

Townsend[28] derived $\tilde{\tau}_{wall,x}/\tilde{\tau}_{wall,z} = 1/100$ using assumptions similar to ours; we then estimate $\lambda_r^x = 100^2\,\lambda_r^z$. Order-of-magnitude considerations yield $k_x = 1$ and $k_z = 0.01$. $\tau = 0.005$ was chosen for computational convenience, since the oscillator time scale is arbitrary.

The period of a two dimensional, uncoupled SL oscillator. Let $\omega_z^+(z^+,t^+) = M(z^+,t^+)\exp(i\phi(z^+,t^+))$, where magnitude $M \in \mathbb{R}$, $M \ge 0$, and phase $\phi \in \mathbb{R}$. In regions where $M(z^+,t^+) \approx M(t^+)$, $\phi(z^+,t^+) \approx \phi(t^+)$, Eq.(3) simplifies to

$$\dot{M} = \left(\sigma_r M - \lambda_r^z M^3\right)\tau, \qquad \dot{\phi} = \left(\sigma_i - \lambda_i^z M^2\right)\tau,$$

such that for $M > 0$, $\lim_{t^+\to\infty} M = A_0 = (\sigma_r/\lambda_r^z)^{1/2}$. An analogous limiting value $\dot{\phi}_\infty = (\sigma_i - (\sigma_r/\lambda_r^z)\lambda_i^z)\tau$ yields the period of the two-dimensional (Tollmien-Schlichting) wave $T = 2\pi/\dot{\phi}_\infty$, where $T = 100\pi$ for our constants. This period is used in the modeling of microgrooves and microvibrations in dolphin chaos control.

Simulation parameters. The equations are solved with a finite-difference, fourth-order, Runge-Kutta solver with time step $dt^+ = 0.2$ and spatial grid $dz^+ = 1$. Harmonic boundary conditions are applied at $z = \pm L/2$ unless noted. When used, side-wall corner boundary conditions $\omega_z^+(\pm L/2,t^+)$ are applied in combination with $\sigma_r = \sigma_r(z^+)$ near the boundary, to obtain $\sigma_r(|z^+| - L/2) \approx \sigma_{r,center}$ and a smooth descent to zero at the boundary $\sigma_r(z^+) = \sigma_{r,center} \times [erf((z^+ + L/2)/25) - erf((z^+ - L/2)/25) - 1]$. The value $\sigma_{r,center}\,(= 1)$ is the σ_r value used for all z when using harmonic boundary conditions. This equation yields a corner boundary layer width of $z^+ \approx 50$, matching Re_{crit}. As a point of interest, it is this side-wall condition that produces the apparent hairpin structures in Fig. 3f. Unless noted, the initial conditions, which embody lateral cellularization due to end effects, are $\omega_z^+(z^+,0) = 0.1\sin(2\pi t^+/200)$, $\omega_x^+(z^+,0) = 10^{-5}N(z^+)$, where $N(z^+)$ are uniformly distributed random numbers with range $(-0.5,0.5)$; N simulates freestream turbulence.

Controlled form of the model. "Controlled" forms of Eqs. (3) and (4) are:

$$\dot{\omega}_z^+ = \left(\sigma\omega_z^+ + \mu^z(z^+,t^+)\frac{\partial^2\omega_z^+}{\partial z^{+^2}} - \lambda^z\omega_z^{+^2}\omega_z^{+^*} - k_x\left|\omega_x^+\right| + I_{ext}^z(z^+,t^+)\right)\tau,$$

$$\dot{\omega}_x^+ = \left(\sigma\omega_x^+ + \mu^x(z^+,t^+)\frac{\partial^2\omega_x^+}{\partial z^{+^2}} - \lambda^x\omega_x^{+^2}\omega_x^{+^*} + k_z\frac{\partial\omega_z^+}{\partial z^+} + I_{ext}^x(z^+,t^+)\right)\tau.$$

Input to the system may be given by spatiotemporally variable diffusion ("μ-control") or external impulse ("I_{ext}-control"). The physical mechanism of μ-control is alteration of the local aspect ratio L_c; this is the source of our claim that variation in μ_r mimics the effect of the surface topology on the flow. The mechanism of I_{ext}-control is the addition of vorticity from a source outside the model, similar to that employed in models of neuron synchronization[21,22].

Shark disorganization control. Uninterrupted riblets are modeled using $\mu^z(z^+) = \mu^x(z^+) = \bar{\mu}\,(1 + \kappa_\mu\sin(2\pi z^+/s^+))$, where $\bar{\mu} = 16(1–0.3i)$ is the flat-plate value. The spacing between riblet peaks $s^+ = 10$ is used unless noted. κ_μ gives the "strength" of the riblets, where the terms "weak" and "strong" for riblets denote $\kappa_\mu = 0.025$ and 0.2, respectively.

Riblets interrupted by the dermal denticles are modeled using $\mu^z(z^+,t^+) = \mu^x(z^+,t^+) = \bar{\mu}\,(1 + \kappa_\mu\sin(2\pi z^+/s^+) + Sc(z^+,t^+) - \overline{Sc})$, where $Sc(z^+,t^+) = (\kappa_\mu/4)|\sin(t^+/200) - \sin(\pi z^+/25)|$, and the overbar denotes an average over a period. The ¼ multiple in the latter equation gives the height of the denticles relative to the riblets.

Dolphin disorganization control. The dolphin's microgrooves[3] are modeled using $\mu^z(t^+) = \mu^x(t^+) = \bar{\mu}\,(1 + \kappa_{groove}\sin(t^+/50))$, where $\kappa_{groove} = 0.075$. Microvibrations[4] are modeled using $I^z_{ext}(t^+) = 0.005(\kappa_{fast}\sin(t^+/800) + \kappa_{slow}\sin(t^+/50))$. Where both microvibration frequencies are applied, $\kappa_{fast} = 1$, $\kappa_{slow} = 1/16$, such that their amplitudes are proportional to the ratio of the periods.

Experimental data source. Fig. 1 pictures clockwise from left sourced or adapted from refs. 19, 24, 25, 3 and 8.

Figs. 3b, 3c, 3e, 3f (upper) sourced from refs. 44, 45, M. Gad-el-Hak (Pvt. Comm.) and 29.

Fig. 4b, 4c, 4f, 4g, 4k, 4l, 4n sourced and adapted from refs. 24, 46, 24, 45, 49, 49 and 50.

Figs. 5a, 5d lower inset, 5e sourced from refs. 25, 25 and 2.

Fig. 6f sourced from ref. 3.

1. Gray, J. Studies in animal locomotion. VI The propulsive power of dolphins. *J. Exp. Biol.* **13**, 192–199 (1936).
2. Adams, M. S. Dermal denticles of tiger shark (*Galeocerdo cuvier*). http://dermaldenticles.blogspot.com/ (Feb26, 2009) Date of access 01/08/2014.
3. Ridgway, S. H. & Carder, D. A. Features of dolphin skin with potential hydrodynamic importance. *IEEE Engrg. in Medicine and Biol.* **12**, 83–88 (1993).
4. Haider, M. & Lindsley, D. B. Microvibrations in man and dolphin. *Science* **146**, 1181–1183 (1964).
5. Phillips, W. R. C. The instability of finite amplitude waves in strong viscid and inviscid shear. In *Mathematical Modeling and Simulation in Hydrodynamic Stability* (ed. Riahi, D. N.) (World Scientific, Singapore), DOI: 10.1142/9789812797308_005 (1996).
6. Carpenter, P. W., Davies, C. & Lucey, A. D. Hydrodynamics and compliant walls: Does the dolphin have a secret? *Current Science* **79**, 758–765 (2000).
7. Babenko, V. V. & Carpenter, P. W. Dolphin hydrodynamics. Chapter 13 in *Flow past Highly Compliant Boundaries and in Collapsible Tubes*, (eds.: Pedley, T. J. & Carpenter, P. W.; Kluwer Academic Publishers, Dordrecht, the Netherlands), 293–323 (2003).
8. Pavlov, V. V. Dolphin skin as a natural anisotropic compliant wall. *Bioinsp. Biomim.* **1**, 31–40 (2006).
9. Gaster, M. Is the Dolphin a Red Herring? In *Turbulence Management and Relaminarisation* (ed. Liepmann, H. W. & Narasimha, R.), *IUTAM Symposium*, Bangalore, India (Springer-Verlag, Berlin), 285–304 (1988).
10. Ptasinski, P. K. *et al.* Turbulent channel flow near maximum drag reduction: simulations, experiments and mechanisms. *J. Fluid Mech.* **490**, 251–291 (2003).
11. Bechert, D. W., Hoppe, G. & Reif, W. E. On the drag reduction of the shark skin. In *AIAA Shear Flow Control Conference,* Boulder, CO, USA, AIAA 85-0546 (AIAA, New York), 1–18 (1985).
12. Choi, K.-S. Near-wall structure of a turbulent boundary layer with riblets. *J. Fluid Mech.* **208**, 417–458 (1989).
13. Dean, B. & Bhushan, B. Shark-skin surfaces for fluid-drag reduction turbulent flow: a review. *Phil. Trans. Roy. Soc. A* **368**, 4775–4806 (2010).
14. Bandyopadhyay, P. R. *et al.* Experiments on the effects of aging on compliant coating drag reduction. *Phys. Fl.* **17**, 085104 (2005).
15. Turing, A. M. The chemical basis of morphogenesis. *Phil. Trans. R. Soc. B* **237**, 37–72 (1952).
16. Meinhardt, H. *Models of Biological Pattern Formation* (Academic Press, London) (1982).
17. Yamaguchi, M., Yoshimoto, E. & Kondo, S. Pattern regulation in the stripe of zebrafish suggests an underlying dynamic and autonomous mechanism. *Proc. Nat. Acad. Sci.* **104**, 4790–4793 (2007).
18. Maini, P. K., Benson, D. L. & Sherratt, J. A. Pattern formation in reaction-diffusion models with spatially inhomogeneous diffusion coefficients. *Mathematical Medicine and Biology* **9**, 197–213 (1992).
19. Nakamasu, A., Takahashi, G., Kanbe, A. & Kondo, S. Interactions between zebrafish pigment cells responsible for the generation of Turing patterns. *Proc. Nat. Acad. Sci* **106**, 8429–8434 (2009).
20. Bandyopadhyay, P. R., Leinhos, H. A. & Hellum, A. M. Handedness helps homing in swimming and flying animals. *Sci. Rep.* **3**, 1128, DOI: 10.1038/srep01128 (2013).
21. Kazantsev, V. B., Nekorkin, V. I., Makarenko, V. & Llinás, R. Self-referential phase reset based on inferior olive oscillator dynamics. *Proc. Nat. Acad. Sci.* **101**, 18183–18188 (2004).
22. Bandyopadhyay, P. R. *et al.* Synchronization of animal-inspired multiple fins in an underwater vehicle using olivo-cerebellar dynamics. *IEEE J. Ocean. Engrg.* **33**, 563–578 (2008).

23. Bandyopadhyay, P. R. & Hansen, J. C. Breakup and then makeup: a predictive model of how cilia self-regulate hardness for posture control. *Sci. Rep.* **3**, 1956, DOI: 10.1038/srep01956 (2013).
24. Falco, R. E. The production of turbulence near a wall. In *AIAA 13th Fluid & Plasma Dynamics Conf.* Snowmass, CO, USA, AIAA 80–1356 (AIAA, New York) (1980).
25. Anderson, M. Dermal denticles of Atlantic sharpnose shark skin; NOAA Teacher at Sea. http://teacheratsea.wordpress.com/tag/dermal-denticles/ (Aug 7, 2011) Date of access 01/08/2014.
26. Hama, F. R., Long, J. D. & Hegarty, J. C. On transition from laminar to turbulent flow. *J. App. Phys.* **28**, 388–394 (1957).
27. Kline, S. J., Reynolds, W. C., Schraub, F. A. & Runstadler, P. W. The structure of turbulent boundary layers. *J. Fluid Mech.* **30**, 741–73 (1967).
28. Townsend, A. A. *The Structure of Turbulent Shear Flow* (Cambridge Univ. Press, New York) (1976).
29. Head, M. R. & Bandyopadhyay, P. New aspects of turbulent boundary layer structure. *J. Fluid Mech.* **107**, 297–338 (1981).
30. Perry, A. E. & Chong, M. S. On the mechanism of wall turbulence. *J. Fluid Mech.* **119**, 173–217 (1982).
31. Bandyopadhyay, P. R. Large structure with a characteristic upstream interface in turbulent boundary layers. *Phys. Fl.* **23**, 2326–2327 (1980).
32. Adrian, R. J., Meinhart, C. D. & Tomkins, C. D. Vortex organization in the outer region of the turbulent boundary layer. *J. Fluid Mech.* **422**, 1–54 (2000).
33. Einstein, H. A. & Li, H. The viscous sublayer along a smooth boundary. *Trans. Am. Soc. Civil Eng.* **123**, 293–313 (1958).
34. Ginzburg, V. L. & Landau, L. D. On the theory of superconductivity. *J. Expt. & Theo. Phys. (USSR)* **20**, 1064 (1950).
35. Albarède, P. & Monkewitz, P. A. A model for the formation of oblique shedding and 'chevron' patterns in cylinder wakes. *Phys. Fl. A* **4**, 744–756 (1992).
36. Pikovsky, A., Rosenblum, M. & Kurths, J. *Synchronization: a universal concept in nonlinear sciences* (Cambridge Univ. Press, Cambridge, England) (2001).
37. Popovich, A. T. & Hummel, R. L. Experimental study of the viscous sublayer in turbulent pipe flow. *AIChE Journal* **13**, 854–860 (1967).
38. Stuart, J. T. On the non-linear mechanics of disturbances in parallel flows, Part 1. The basic behavior in plane Poiseuille flow. *J. Fluid Mech.* **9**, 353–370 (1960).
39. Watson, J. On the non-linear mechanics of disturbances in parallel flows, Part 2. The development of a solution for plane Poiseuille flow and for plane Couette flow. *J. Fluid Mech.* **9**, 371–389 (1960).
40. Noack, B. R., Ohle, F. & Eckelmann, H. On cell formation in vortex streets. *J. Fluid Mech.* **227**, 293–308 (1991).
41. Bandyopadhyay, P. R. & Hellum, A. M. Llinás phase reset mechanism delays the onset of chaos in shark and dolphin wall turbulence. *NUWC-NPT Tech. Rept. 12,154* (Naval Undersea Warfare Center, Newport, RI, USA) (2014).
42. Haller, G. Exact theory of unsteady separation for two-dimensional flows. *J. Fluid Mech.*, **512**, 257–311 (2004).
43. Bandyopadhyay, P. R. A low dimensional structural model of a turbulent boundary layer separating intermittently in space. *NUWC-NPT Tech. Rep. 10,400* (Naval Undersea Warfare Center, Newport, RI, USA) (1994).
44. Kegelman, J. T., Nelson, R. C. & Mueller, T. J. The boundary layer on an axisymmetric body with and without spin. *AIAA J.* **21**, 1485–1491 (1983).
45. Perry, A. E., Lim, T. T. & Teh, E. W. A visual study of turbulent spots. *J. Fluid Mech.* **104**, 387–405 (1981).
46. Sewell, T. & Waldron, M. Dermal denticles of great white shark. Electron Microscope Unit, University of Cape Town, Smithsonian Museum of Natural History, http://ocean.si.edu/ocean-photos/biomimicry-shark-denticles (Apr16, 1997) Date of access 01/08/2014.
47. Hof, B., Westerweel, J., Schneider, T. M. & Eckhardt, B. Finite lifetime of turbulence in shear flows. *Nature* **443**, DOI: 10.1038/nature05089 (2006).
48. Du, Y. & Karniadakis, G. E. Suppressing wall turbulence by means of a transverse traveling wave. *Science* **288**, 1230–1234 (2000).
49. Liu, Z.-C., Adrian, R. J. & Hanratty, T. J. A study of streaky structures in a turbulent channel flow with particle image velocimetry. *8th Intl. Sympo. on Applications of Laser Techniques to Fluid Mechanics,* Lisbon, Portugal (1996).
50. Forest, J. B. The wall pressure spectrum of high Reynolds number rough-wall turbulent boundary layers. MS Thesis (VPI&SU, Blacksburg, , VA, , USA) (2012).
51. Brown, G. L. & Thomas, A. S. W. Large structure on a turbulent boundary layer. *Phys. Fl.* **20**, S243–S252 (1977).
52. Bandyopadhyay, P. R. & Hussain, A. K. M. F. The coupling between scales in shear flows. *Phys. Fl.* **27**, 2221–2228 (1984).
53. Marusic, I., Mathis, R. & Hutchins, N. Predictive model for wall-bounded turbulent flow. *Science* **329**, 193–196 (2010).
54. Phillips, W. R. C. On a class of unsteady boundary layers of finite extent. *J. Fluid Mech.* **319**, 151–170 (1996).
55. Wu, X. & Moin, P. Direct numerical simulation of turbulence in a nominally zero-pressure-gradient flat plate boundary layer. *J. Fluid Mech.* **630**, 5–41 (2009).
56. Alfredsson, P. H., Johansson, A. V., Haritonidis, J. H. & Eckelmann, H. The fluctuating wall-shear stress and the velocity field in the viscous sublayer. *Phy. Fl.* **31**, 1026–1033 (1988).

Acknowledgments

Support of this research came from the Office of Naval Research, Biology-Inspired Autonomous Systems Program (ONR 341), to P.R.B. A.M.H. was supported by an ASEE-ONR Postdoctoral Fellowship.

Author contributions

The self-regulation framework of wall-turbulence control was synthesized by P.R.B. over decades. AMH contributed to the oscillator tuning and assisted in manuscript preparation. P.R.B. supervised A.M.H.

Additional information

Supplementary information accompanies this paper at http://www.nature.com/scientificreports

Competing financial interests: The authors declare no competing financial interests.

How to cite this article: Bandyopadhyay, P.R. & Hellum, A.M. Modeling how shark and dolphin skin patterns control transitional wall-turbulence vorticity patterns using spatiotemporal phase reset mechanisms. *Sci. Rep.* **4**, 6650; DOI:10.1038/srep06650 (2014).